# Identifying Adhesion Properties at Si/Polymer Interfaces with ReaxFF

Manav Bhati and Thomas P. Senftle*

Department of Chemical and Biomolecular Engineering, Rice University, 6100 Main Street, Houston, Texas 77005-1892, United States

Ⓢ *Supporting Information*

ABSTRACT: High capacity lithium-ion battery anodes based on silicon (Si) undergo large volume fluctuations during operation that can compromise the structural integrity of the electrode. This issue can be mitigated by using flexible polymers to encapsulate the active Si material so that the electrode can accommodate significant volume expansion and contraction during battery cycling. Such designs require a stable interface between the polymer and Si that can undergo repeated deformations. To help design such interfaces, we have developed a ReaxFF force field to investigate the interfacial adhesion properties of polymers on Si surfaces at the atomistic scale. We consider three C/N/H-based polymers in this study that have been shown to improve battery performance when used as a binder for the active Si component in battery electrodes: polyacrylonitrile (PAN), pyrolyzed PAN (PPAN), and polypyrrole (PPy). Molecular dynamics simulations with the newly developed ReaxFF parameters show that single chains of PPy bind more strongly to Si compared to those of PAN or PPAN, which is validated by adsorption energies computed with density functional theory. This trend reverses when considering the interface between bulk polymers and Si, with bulk PPy binding least strongly to the surface. We show that this reversal is caused by the interaction of individual polymer chains at the interface, where the first layer of PPy binds so strongly that it prevents the next layer of chains from accessing the surface. This work offers insight into atomistic interfacial phenomena in composite electrode materials and provides simulation tools that can be readily extended to other Si/polymer systems.
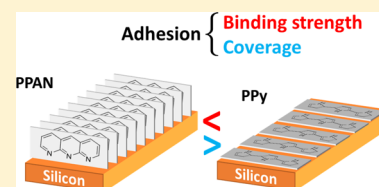
1. INTRODUCTION

Stable silicon/polymer interfaces are crucial for the performance of high capacity Li-ion batteries that use Si as the active Li-storing material.[1,2] Si anodes have a high theoretical Li capacity of 3579 mA h g^{-1}, but their use is hampered by a ~300% volume expansion during lithiation that causes rapid degradation of the electrode.[3,4] This issue can be alleviated by embedding particles of the active material in an adhesive matrix, such as a polymer binder, that can accommodate large volume changes during lithiation and delithiation (Figure 1). This prevents pulverization of the active material, isolation and agglomeration of active particles, and rupture of the solid electrolyte interphase (SEI) layer.[5−9] Adhesive binders also can act as an artificial passivation layer that protects the electrolyte from continuous decomposition and irreversible capacity loss.[10,11] The improved mechanical integrity also helps to maintain channels that promote electrical and ionic conductivity.[12] Polyvinylidenefluoride (PVDF), which is the most commonly used polymer binder, works well in graphite anodes (~13% volume expansion),[13] but fails in Si anodes because of poor adhesion to Si surfaces.[14] Thus, identifying polymers that form strong and stable interfaces with Si is essential for the development of next-generation battery anodes.

Several research efforts have aimed at enhancing the adhesive, elastic, electrical, and ionic properties of binders for use in Si anodes.[1,2,15−19] In this work, we focus on the adhesive properties of polymer binders on Si surfaces, which is necessary for understanding how polymers can be used to maintain a flexible mechanical network throughout the electrode during cycling. In particular, we investigate the properties of three polymer binders that have been demonstrated to yield enhanced performance in Si-based batteries: polyacrylonitrile (PAN), pyrolyzed PAN (PPAN), and polypyrrole (PPy). Numerous studies demonstrate that PAN can be an effective binder in Si, graphite, and Li$_4$Ti$_5$O$_{12}$ (LTO) anodes.[10,20,21] The polarity of the nitrile groups in PAN yields high binder coverage and strong adhesion to the Si surface, which results in better electrochemical performance than conventional PVDF and sodium carboxymethyl cellulose (CMC) binders.[10,21] Other than being a strong adhesive, PAN also forms an artificial surface passivation layer that helps reduce the initial loss of electrolyte through irreversible decomposition.[10] PPAN, also known as cyclized PAN, is a derivative of PAN formed via pyrolysis that has been used as a binder for Si anodes in several studies.[22−26] The aromatic nature of PPAN leads to enhanced conductivity compared to PAN. Conductive polymers are advantageous in eliminating the use of conductive additives, which improves the specific capacity of the battery.[17] Biswal and co-workers[22] reported an inexpensive method for synthesizing micron-sized porous Si particles that achieve enhanced battery performance when mixed with PPAN, achieving a capacity of 1000 mA h g^{-1} for
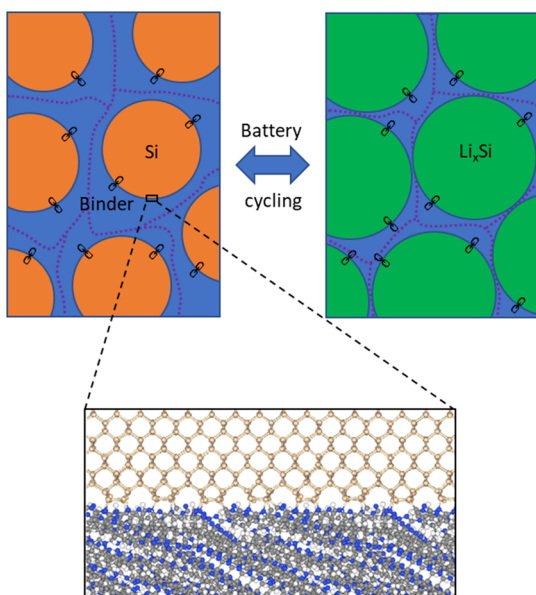
Figure 1. Schematic representation of an idealized Si/binder anode during battery cycling. Si particles (orange) and expanded Li$_x$Si particles (green) remain connected to the polymer binder (blue) because of strong interfacial bonds (black linkages) that persist over repeated volume fluctuations. Conduction channels (purple) are retained throughout cycling, which preserves battery performance. Inset shows an enlarged illustration of the interfacial region between Si and the polymer binder at the atomistic scale, which is the focus of this study.

600+ cycles. Micron-sized Si particles typically induce high stress and suffer from increased pulverization compared to their nanosized counterparts,[6,27] which underscores the capability of PPAN for alleviating stress in Si anodes. In another study, Piper et al.[25] synthesized electrodes from a hierarchical porous framework of Si nanoparticles coated with PPAN, which yields only ∼23% volume expansion after 20 cycles demonstrating that PPAN can accommodate up to ∼300% volume expansion of Si. PPy has also shown potential as a conductive binder and coating in Si anodes.[28−33] Chew et al.[30] used a chemical polymerization method to synthesize nano-Si/PPy composite anodes, which showed significantly better cycling stability and capacity retention compared to bare Si anodes. In another study, Du et al.[29] synthesized PPy-coated porous hollow silicon (PHSi) nanospheres, which showed 88% reversible capacity retention after 250 cycles, showing better cycling stability than bare PHSi. Strong adhesion between the PPy coating and PHSi enhanced surface electric conductivity and improved structural integrity of the composite. However, PPy coatings on Si nanoparticles have also been shown to cause self-discharging or self-delithiation in the anode material because of compressive stress generated by the constraining effects of the hard and thick PPy coating layer.[34] PAN is also considered to be a stiff binder, which can lower anode capacity by inhibiting volume expansion of the active material.[10] PAN, PPAN, and PPy have all shown promising electrochemical performance, but the underlying bonding behaviors and interfacial properties responsible for this enhanced performance are not well understood in many instances.

Selecting the best binder for a particular active material is crucial for optimizing battery performance. This is a challenging task, as interfacial properties are influenced by several interrelated phenomena at the active material/binder interface. Interfacial characterization techniques provide information about the chemical composition and strength of the interface but are limited in their ability to provide atomistic-scale knowledge regarding binding mechanisms at the interface. Computational simulation tools can provide insight into such interfacial phenomena, which can inform tailoring strategies for optimizing the properties of Si/binder composites. Many studies have employed density functional theory (DFT) to determine the adhesion energies of active material/binder systems.[35−38] However, such simulations are limited by the computational expense of quantum-based calculations and often cannot provide a complete picture of bulk interfacial phenomena. Continuum scale simulations, on the other hand, provide knowledge of macroscale properties,[34,39−41] but cannot reveal the nature of binding or the interfacial composition at the atomistic scale. To bridge this gap, reactive molecular dynamics (MD) simulations with atomistic force fields are well-suited for predicting adhesion energies, atomistic composition, and binding mechanisms at interfaces. Although MD simulations have been used in various studies to understand the interfacial phenomena of polymers with silica,[42−44] carbon nanotubes,[45,46] and graphene,[47] only a few studies have investigated such interfaces in the context of battery binder materials (e.g., PVDF/graphite[48] and PVDF/copper[49] interfaces).

In this study, we applied the ReaxFF[50] reactive force field to understand Si/polymer interfaces. ReaxFF has a bond-order formalism that allows the formation and dissociation of chemical bonds during a simulation, which has been successfully applied in many studies assessing battery materials. Raju et al.[51] developed a Li/C ReaxFF force field to understand the intercalation mechanism of Li in carbon-based anodes, for which they obtained voltage profiles in good agreement with experiments. Several studies have applied ReaxFF to investigate lithiation mechanism in Si-based materials, including Si nanowires,[52] SiO$_x$ nanowires,[53] carbon-coated Si/SiO$_x$ nanostructures,[54] and SiO$_2$/Al$_2$O$_3$ coating layers.[55] The structural evolution of Si anodes and their mechanical properties as a function of Li concentration have been studied extensively using ReaxFF.[56−58] ReaxFF has also been used to study the electrolyte/electrode interfacial phenomena leading to SEI formation and evolution,[59−61] and the interfacial adhesion phenomena of polymers on silica glass.[42,43] Finally, Saha et al.[62,63] applied ReaxFF to investigate the carbonization mechanism for the formation of carbon fibers from PAN. These studies demonstrate that ReaxFF is an ideal tool for studying Si/polymer interfaces.

Here, we developed a Si/C/N/H ReaxFF force field to investigate the adhesive properties of three C/N/H-based polymer binders (PPAN, PAN, and PPy) with Si surfaces. We first evaluated the mechanical properties of the bulk polymers (i.e., bulk density and Young's modulus) to validate the C/N/H force field parameters. The interaction of the three polymers with Si was then studied to gain comprehensive insights into the interfacial binding properties. We find that the three polymers exhibit unique adhesion energies and bonding characteristics that depend on the structure of the polymer. Monomers and single chains of PPy bind stronger to the Si surface than those of PPAN and PAN yet, bulk PPy exhibits the weakest binding to the Si surface. Simulation analyses reveal that this difference in the binding strength arises from interactions between the polymer chains near the Si surface. PPy chains near the Si surface bind strongly in a parallel

orientation that block the next layer of polymer chains from accessing binding sites on the surface, thus reducing the overall adhesion. Such atomistic scale knowledge of the binding mechanism provides strategies to improve the performance of high capacity Li-ion batteries, such as enhancing polymer binding through backbone modification to minimize steric crowding at the interface.

2. COMPUTATIONAL METHODS

2.1. Force Field Development. The ReaxFF force field[50] is based on a bond order formalism that allows covalent bonds to dynamically form and break during the course of a simulation. ReaxFF also employs the electronegativity equalization method[64] to calculate instantaneous partial charges on all atoms in the system. The full functional form of ReaxFF is described in Chenoweth et al.[65] and a review of ReaxFF applications is provided by Senftle et al.[66] The parameters for the Si/C/N/H force field developed in this study were obtained by merging parameters from previous C/N/H,[62] Si/C/H,[67] and Si/N/H (private communication with van Duin) force fields and the merging procedure has been described in detail in Section 1.1 of the Supporting Information. Si/N bond and Si/N/C valence angle parameters were developed in this study using a training set generated with DFT, where the parameter values were optimized using an iterative single-parameter parabolic optimization scheme.[68] The new parameters are provided in Tables S2−S4 of the Supporting Information.

Training data for parameter optimization was generated using both plane-wave and atom-centered DFT simulation packages; the full training set is included in the Supporting Information. This set includes Si/N bond dissociation energy curves for 13 molecules and Si/C/N valence angle energy curves for 22 molecules, which were calculated using NWChem 6.8.[69] The DFT calculations applied the B3LYP hybrid functional[70] with triple-zeta 6-311G** atom-centered basis sets. van der Waals interactions were treated with Grimme's D3 empirical dispersion correction.[71] Total electronic energies were converged to 5×10^{-6} hartree. Structures were optimized using a conjugate gradient algorithm, where forces were converged to 4.5×10^{-4} au$_f$. The comparison of DFT and ReaxFF bond dissociation energy curves and valence angle energy curves are shown in Figures S1 and S2,. ReaxFF accurately reproduces these curves for molecules containing Si−C and Si−N single and double bonds. Higher deviations are present for molecules containing triple bonds (e.g., CH≡Si−NH$_2$ and CH$_3$−Si≡N), as lower weights were placed on these molecules during the parameter optimization procedure because these bond conformations do not appear in our MD simulations. Overall, a reasonable agreement is achieved between DFT and ReaxFF, especially near equilibrium bond lengths and valence angles because higher training weights were applied on those data points. The geometries away from equilibrium have much higher energies and are less significant in the simulations, and as such lower training weights were applied on those structures leading to higher deviations between DFT and ReaxFF. In addition, DFT is known to exhibit accuracy issues along bond-dissociation energy curves, which are much better described by multireference ab initio methods.[72] However, DFT does perform better when describing the potential energy surface closer to equilibrium bond distances. For this reason, we do not anticipate that the deficiencies of DFT will impact our current

study, where we do not observe bond breaking events in the polymer chains during our simulations. Further discussion on the limitations of the developed force field is provided in detail in Section 1.2.1 of the Supporting Information.

Training data for the adsorption of C/N/H-containing molecules on the Si surface and for the interstitial adsorption of N in bulk Si were generated using the Vienna ab initio simulation package (VASP 5.4.4).[73] This data included the adsorption energies of eight molecules on a reconstructed (4 × 2) Si(100) slab that comprised six Si layers. The reconstructed Si(100)[74] surface structure was obtained by relaxing the as-cleaved structure of the Si(100) surface to form asymmetrically buckled Si dimers on the surface. The number of layers was chosen by converging adsorption energies to within 1 meV. The bottom layer of Si was passivated with H atoms to saturate Si dangling bonds and the bottom two Si layers and the H-passivation layer were frozen. All calculations were spin-polarized and applied the Perdew−Burke−Ernzerhof exchange correlational functional[75] with projector-augmented-wave potentials.[76] The atom valences that were treated self-consistently for Si, C, N, and H were $3s^23p^2$, $2s^22p^2$, $2s^22p^3$, and $1s^1$, respectively. Energy convergence tests were used to determine a kinetic energy cutoff of 450 eV and a Monkhorst−Pack[77] k-point mesh of 2 × 4 × 1. Gaussian smearing was applied with a smearing width of 0.01 eV. Grimme's D3 empirical dispersion correction[71] was applied to approximate van der Waals interactions. Geometries were optimized until the forces converged to within 0.05 eV Å^{-1}. The molecular adsorption energies and interstitial adsorption energy of N in Si obtained from DFT and ReaxFF calculations are presented in Tables S5 and S6, respectively, where the ReaxFF values have an average deviation of 8.8 and 3.2 kcal/mol, respectively, from their DFT counterparts. In general, the cyclic aromatic molecules with two N atoms in the ring, (e.g., pyrazole and imidazole) had higher deviation in their adsorption energies, as these molecules do not appear in our simulations and thus had lower training weights. The reasonable agreement between DFT and ReaxFF signifies the accuracy of the trained force field parameters for their use in this study.

2.2. MD Simulations. MD simulations were performed using the Large-scale Atomic/Molecular Massively Parallel Simulator (LAMMPS, 12 Dec 2018 version)[78] and the Si/C/N/H ReaxFF force field developed in this study. The Nose−Hoover[79] thermostat and the barostat with the damping parameters of 100 and 1000 fs, respectively, were used to maintain temperature and pressure in all MD simulations. A timestep of 0.25 fs was used for the time integration of the Verlet[80] equations of motion. All results reported herein were obtained by averaging five independent trial MD simulations constructed with different initial geometries and velocities.

Each simulation employed polymer structures with a chain length of 20 monomers (Figure 2). As shown in Table S7, the mechanical properties of the polymers did not change considerably for longer chains with 50 monomers. Experimentally, the structure of PAN evolves as it is thermally treated during pyrolysis. Several structures and reaction mechanisms have been proposed in the literature for the complicated pyrolysis process.[81,82] In this study, we adopt the widely-used[62] cyclized six-membered aromatic structure to represent PPAN, as shown in Figure 2a.
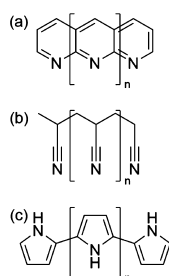
Figure 2. Representative polymer structures of (a) PPAN, (b) PAN, and (c) PPy binders. Polymer chains of 20 monomers were employed for all three binders.

3. RESULTS AND DISCUSSION

3.1. Mechanical Properties of Polymer Binders. We determined the equilibrium density of each polymer prior to building models of the polymer/silicon interface. The simulation workflow for these calculations is outlined in Figure 3. First, 25 polymer chains were placed randomly in a
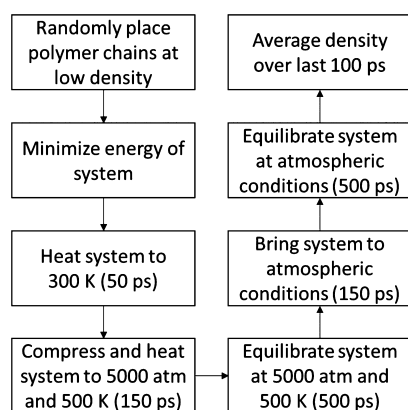
Figure 3. Simulation workflow for determining the density of the polymer binders.

simulation cell at a low density of 0.01 g cm^{-3} followed by an energy optimization via a conjugate gradient minimization of forces. The temperature of the relaxed system was then raised from 0.1 to 300 K by a uniform temperature ramp over 50 ps in an *NVT* ensemble. A compressed polymer structure was obtained by linearly increasing the pressure and temperature of the system to 5000 atm and 500 K, respectively, over a 150 ps timeframe in an *NPT* ensemble. The system was then equilibrated at the constant pressure (5000 atm) and temperature (500 K) for 500 ps. The pressure and temperature were then reduced linearly in the next 150 ps to 1 atm and 300 K, which yields the density of the binder under atmospheric conditions. The system was then allowed to equilibrate for 500 ps under these conditions, and the average density was

determined from the last 100 ps of the simulation. The average density calculated from five trials for each binder and the standard error is tabulated in Table 1, along with density values collected from the literature for comparison. A good agreement can be seen between the densities calculated in this study with those reported in the literature with maximum variations within ~2%.

The Young's moduli of the three polymers were also calculated to validate the accuracy of the C/N/H force field. Bulk binders were generated from a simulation cell containing 40 polymer chains using the same method as was used for determining the polymer density. Five sample geometries were extracted from the last 125 ps of the equilibrated *NPT* simulations at 1 atm and 300 K. These samples were then stretched uniaxially in *x*, *y*, and *z* directions (one direction at a time) at a constant strain rate of 10^9 s^{-1}. Because the samples were deformed in one direction, they were allowed to relax in the other two directions to capture the Poisson effect.[88] The resulting stress–strain curves were averaged over the three directions and over five repeated runs with independent initial structures to obtain the Young's modulus from the slope of the curve in the elastic linear regime. The average stress–strain curve for each of the three polymers is shown in Figure 4. A zoomed-in view of the elastic regimes of these curves and a description of the numerical method used to determine the linear elastic regime are described in the Supporting Information (Figure S4). The average Young's modulus obtained from each curve and literature comparisons are presented in Table 1. The computed Young's moduli have the same order of magnitude and are in close agreement with the literature values, thus validating our simulation methodology and the C/N/H parameters.

3.2. Si/Polymer Interface. In the following section, we investigate the properties of Si/polymer interfaces for various structural forms of the polymer to gain a comprehensive understanding of interfacial adhesion mechanisms. The adhesion energy of the interface between Si and the polymer was calculated using eq 1

$$E_{\text{adhesion}} = E_{\text{Si/binder}} - E_{\text{binder}} - E_{\text{Si}} \tag{1}$$

where the adhesion energy (E_{adhesion}) is defined as the difference in the energy of the composite system ($E_{\text{Si/binder}}$) and the individual component energies of the binder (E_{binder}) and the Si slab (E_{Si}). These energies are calculated from single-point snapshots of the respective geometries extracted from the MD simulation. The energies do not include relaxation of the Si or binder slabs when the interface is broken and thus isolate the instantaneous bond strength at the interface. Negative values of E_{adhesion} signify strong binding at the interface.

We first investigated the binding characteristics of single polymer chains on the Si surface. MD simulations were performed in an *NVT* ensemble at 300 K, where the simulation cell contained a single polymer chain over a (20 × 20) Si slab

Table 1. Density and Young's Modulus of PPAN, PAN, and PPy Calculated in This Study and from the Literature[a]

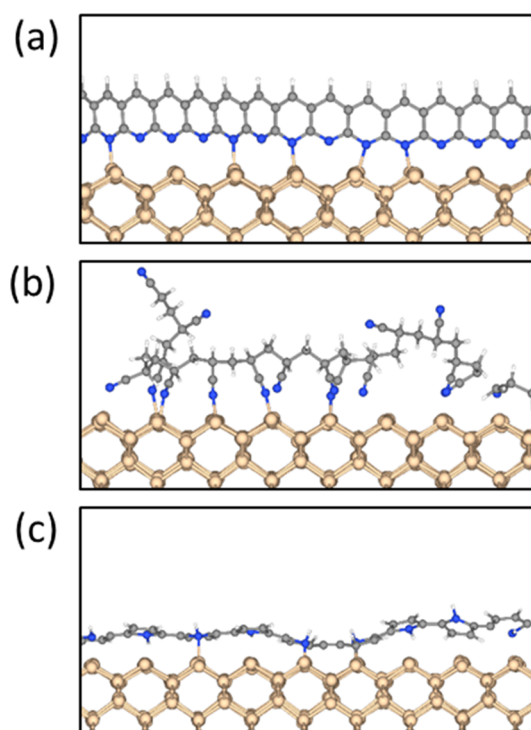| binder	density (g cm^{-3})		Young's modulus (GPa)	
	this study	literature	this study	literature
PPAN	1.433 ± 0.012	1.34−2.1[62,83]	1.184 ± 0.071	1.34[83]
PAN	1.203 ± 0.004	1.23[84]	6.002 ± 0.048	6.3[85]
PPy	1.263 ± 0.007	1.25[86]	2.059 ± 0.026	1.2−3.2[87]

[a]References[83,85,87] are from experimental studies and refs[62,86] are from computational studies.
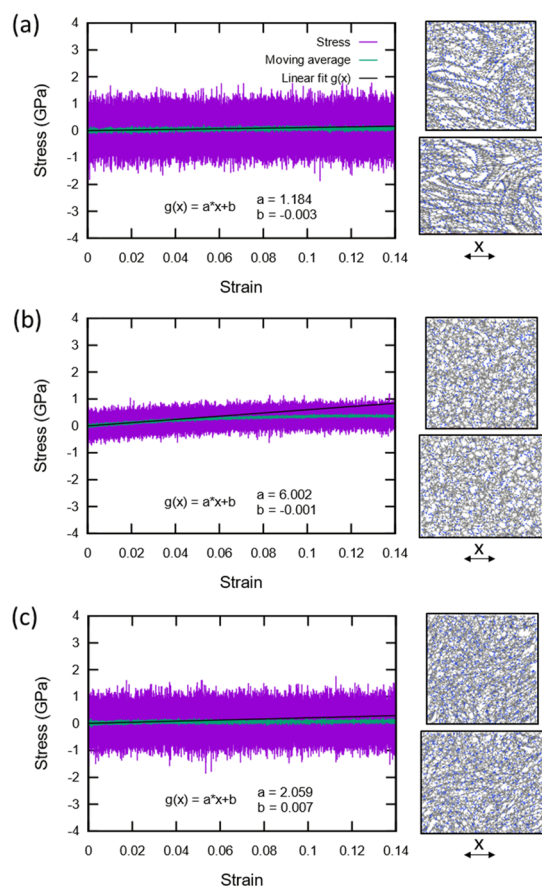
Figure 4. Average stress−strain curves of (a) PPAN, (b) PAN, and (c) PPy. Insets on the right are the initial relaxed (top) and the final stretched (bottom) snapshots from MD simulation of tensile stretching in the *x* direction. (Blue: N, gray: C, and white: H).

Figure 5. Snapshots from MD simulations of single polymer chains of (a) PPAN, (b) PAN, and (c) PPy on the Si(100) surface. PPAN and PAN bind perpendicular to the surface, and PPy binds parallel to the surface. These snapshots were taken after the systems reached equilibration after ∼1000 ps. (Beige: Si, blue: N, gray: C, and white: H).

with 24 layers (i.e., 9600 Si atoms). The dimensions of the cell were 76.46 Å × 76.46 Å × 150.0 Å. Five independent initial geometries were created by randomly placing the PAN, PPAN, or PPy single chains over the Si surface The trajectories from MD simulations show different binding modes for these polymers on the surface, as shown in Figure 5. PPAN and PAN chains bind such that their monomer rings stand perpendicular to the Si surface, where the polymer is attached through N−Si bonds. PPy binds parallel to the Si surface, such that both C−Si and N−Si bonds are formed. The number of instantaneous bonds is determined directly from ReaxFF bond orders, where a bond order cutoff of 0.3 was used to determine if there is a bond between two atoms. The Si/polymer geometry snapshots were extracted at 25 ps intervals from the MD trajectories, and the adhesion energies were calculated via eq 1. The simulations were performed until fluctuations in adhesion energy plateaued to a constant average value, which signaled that the system had equilibrated to a stable geometry. The average adhesion energies of five equilibrated geometries for each polymer are shown in Figure 6 with respective standard errors. These data demonstrate that single chains of PPy bind more strongly to the Si surface compared to PPAN and PAN.

The interaction between bulk polymers and the Si surface was modeled using an (8 × 8) mirrored Si slab consisting of 24 Si layers (i.e., 1536 Si atoms). First, each bulk polymer structure was generated in a simulation cell with final cell dimensions of 30.57 Å × 30.57 Å × 30.57 Å that would fit perfectly on the Si slab along the *z* direction. The number of

polymer chains in the simulation cell for each binder was determined from the densities calculated in Section 3.1. The corresponding number of chains was randomly placed in the simulation cell at a low initial density of 0.01 g cm^{-3}, and the simulation procedure summarized in Figure 7 was followed to build the bulk polymer and its interface with Si. Boundaries of the polymer simulation cell were periodic in the *x* and *y* directions and were nonperiodic/reflective in the *z* direction (to create an artificial interface that can be replaced with the Si slab). The cell was deformed at a constant strain rate of 3 × 10^9 s^{-1} in all three directions simultaneously until the correct cell dimensions were obtained. Once the bulk polymer slab was built, it was then placed next to the Si slab along the *z* direction with a separation of 2.2 Å between the slabs, as shown in the left image of Figure 6b. The energy of the composite system was then minimized using the conjugate gradient method prior to MD simulations.

Adhesion energies were calculated from fully periodic MD simulations in the *NVT* ensemble at 300 K, where energies were computed at 25 ps intervals using eq 1. Once the adhesion energies and the Si/polymer interface stabilized, the pressure on the simulation cell was linearly increased to 5000 atm in all the three directions independently. This high pressure was maintained until the adhesion energies equilibrated, and then, the pressure was reduced linearly to 1 atm in all directions. Finally, the composite system was equilibrated at 1 atm and 300 K until large fluctuations in the adhesion energy dissipated. The high-pressure *NPT* simulations were performed to eliminate artifacts arising from the initial separation of 2.2 Å between the Si surface and the binder. Representative initial and final geometries of these Si/bulk polymer simulations are
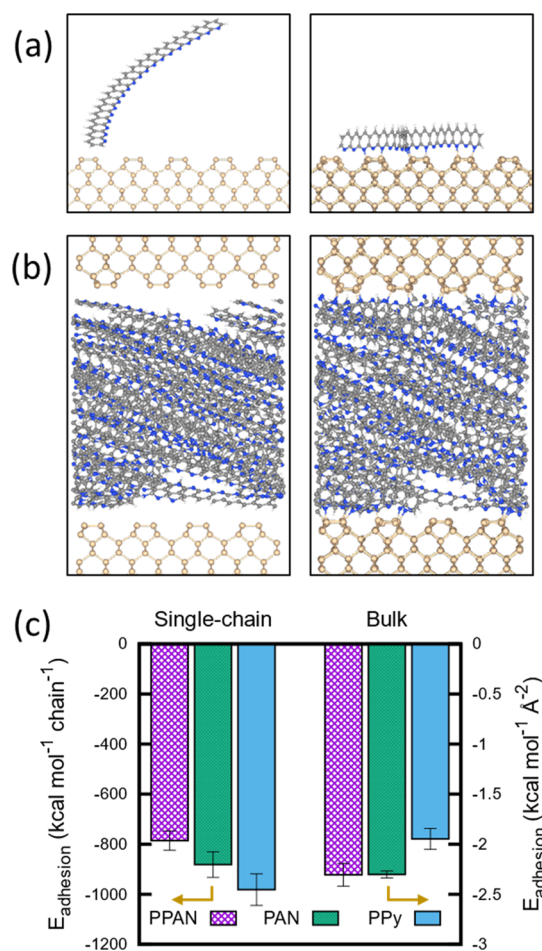
Figure 6. Snapshots from MD simulations of (a) single chain PPAN and (b) bulk PPAN over the Si(100) surface. Left and right panels are the initial and final geometry configurations, respectively. Final geometry snapshots for single chain and bulk polymer cases were taken after the systems equilibrated at ~1000 and ~4000 ps, respectively. (c) Adhesion energy of the three polymers with Si for single chain polymer and bulk polymer cases. Error bars indicate the standard error over five independent simulations, where each simulation had a different initial geometry. (Beige: Si, blue: N, gray: C, and white: H).
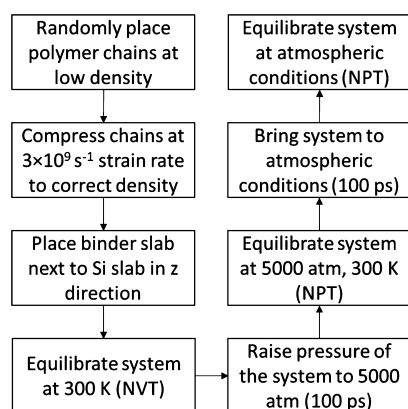

Figure 7. Simulation workflow for building the Si/bulk polymer interface.

shown in Figure 6b. To account for variations in the chain alignment at the interface, five trials of the Si/bulk polymer interfaces were simulated for each polymer, where the

adhesion energy from each trial was determined from the equilibrated value taken at the end of each simulation. The average adhesion energies for bulk polymers with Si are shown in Figure 6c, where it is evident that they do not exhibit the same binding trend as was observed for the single chains. Notably, bulk PPy now has a lower adhesion energy compared to PPAN and PAN.

DFT simulations were performed to validate the observations from the MD simulations of the single chain polymers on Si(100). We use pyridine and pyrrole (i.e., the monomers of PPAN and PPy) to investigate electronic binding properties at the Si/polymer interface. For each monomer, 11 geometries were constructed by changing the orientation of the monomer and its adsorption site on the reconstructed (4 × 4) Si(100) slab. Details of the geometries are provided in Figures S5 and S6. These calculations were performed using VASP 5.4.4 with the same settings as described in Section 2.1, except that the k-point mesh for sampling the Brillouin zone was 2 × 2 × 1. The most stable adsorption geometry of each monomer is shown in Figure 8. Pyridine binds perpendicular to Si through a dative
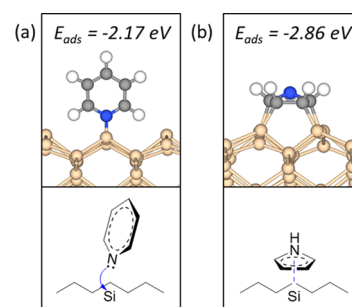
Figure 8. Most stable configurations obtained from DFT calculations and the respective Lewis structures of (a) pyridine and (b) pyrrole on the Si(100) surface. (Beige: Si, blue: N, gray: C, and white: H).

N−Si bond, and pyrrole binds parallel to Si through multiple C−Si bonds. For pyridine, another stable configuration (a half-bent ring) was also observed, but such a configuration was found to be energetically unfavorable for a polymer chain (see Figure S7). The most stable configurations of the monomers on the Si surface determined by DFT have the same binding mechanisms and adsorption energy trend as those predicted by the MD simulations for single chain polymers. Note that the magnitude of adsorption energies should not be compared with adhesion energies of single chain polymers because (1) the monomers are structurally different from polymer chains and (2) the adsorption energy is calculated with reference to an energetically relaxed structure of the monomer, whereas the adhesion energy is calculated with reference to the adsorbed structure of the polymer chain. These structures were not explicitly included in the ReaxFF training set, and as such the good agreement between DFT and MD simulations validates the applicability of the parameters used in this study.

The differences in binding mechanisms in pyridine and pyrrole originate from the dissimilar electronic environments of nitrogen in each monomer, as is depicted by the Lewis structures in Figure 8. The lone pair in pyridine can form a dative bond with Si without compromising the conjugation in the aromatic ring, whereas the lone pair in pyrrole is not available for dative bonding because it is delocalized throughout the aromatic ring. The aromaticity of pyrrole is disrupted as the molecule approaches the surface, which allows

each carbon atom in the pyrrole ring to adapt a stable sp^3 binding configuration on the Si surface. With DFT simulations justifying the adhesion energy trend and binding mechanisms of single chain polymers on the Si surface, we have formulated two hypotheses that together account for the reversal of the adhesion energy trend observed for the bulk polymer case:

1. Chains derived from the bulk polymer will have a binding mechanism and orientation that is similar to what was observed for the polymer single chains on the Si surface. PPAN chains orient themselves perpendicular to the surface, and PPy chains orient themselves parallel to the surface.

2. The perpendicular orientation of PPAN chains allows for better alignment that permits stacking of more chains at the interface. Fewer PPy chains can access the surface because each PPy chain lies parallel to the surface, which leads to weaker overall adhesion.

These hypotheses are tested below with simulations of polymer chains at varying coverages over the Si surface, along with structural analyses of MD trajectories of the Si/bulk polymer system.

Simulations of polymer layers on the Si surface were performed to study how adhesion energies and binding characteristics evolve as the surface coverage of polymer chains is increased. For each polymer, layers having coverage of five (C5), ten (C10), and fifteen (C15) polymer chains on the Si surface were constructed. The Si slab and the simulation cell were similar to the ones used in Si/single chain polymer simulations. For each coverage, four independent geometries were simulated using the *NVT* ensemble at 300 K. The representative initial and final geometries of the system are shown in Figure 9a,b. The average adhesion energies per chain calculated at the end of the simulations are shown in Figure 9c. C5 exhibits a binding strength order as was observed for single chain polymers (Figure 6c), where PPy binds more strongly than PPAN and PAN. The binding strength order reverses as the coverage increases from C5 to C15 and approaches that of the bulk polymers with PPy binding more weakly than PPAN and PAN.

The structure of the bonded polymer chains was analyzed to understand the transition of the adhesion energy trend as coverage is increased from C5 to C15. The average orientation angle of PPAN and PPy polymer chains was calculated and is presented in Table 2. The orientation angle, as described in Figure 10, is defined as the angle between the z axis that is normal to the Si surface and the axis that is normal to the plane of the monomer ring. We find that the perpendicular orientation of PPAN and the parallel orientation of PPy are maintained at all coverages, strengthening our first hypothesis that the bulk polymer chains would have orientations similar to that of the single chains. The PPAN orientation angle approaches 90° (i.e., perpendicular to the surface) as the coverage increases, which demonstrates that PPAN can achieve closer packing and higher chain density on the surface. PPy chains orient parallel to the surface, which occupies more area per chain compared to the perpendicular arrangement of PPAN.

Fewer PPy chains are able to adhere to the surface because the surface quickly becomes crowded. The effective number of chains bound to the surface can be calculated by taking the ratio of the adhesion energy of the entire polymer layer to that of a single chain. In a hypothetical case of 100% adsorption, all
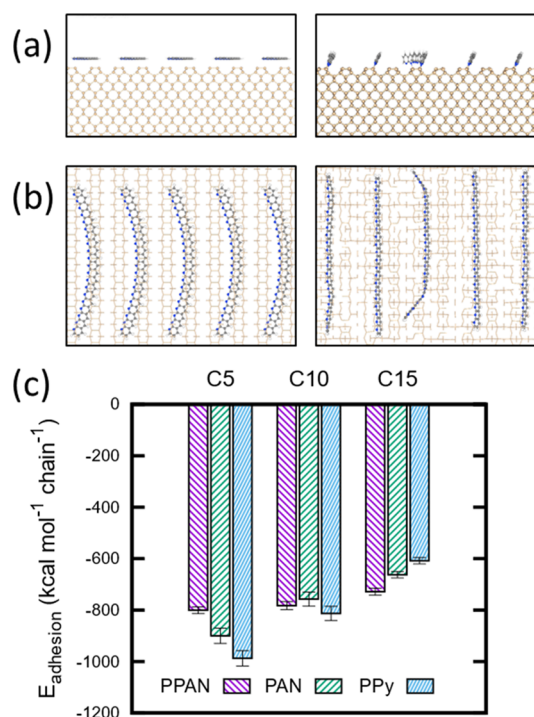
Figure 9. (a) Side view and (b) top view of snapshots from MD simulations of the PPAN layer with a coverage of five chains (C5) on Si(100). Left and right panels are the initial and final geometry configurations, respectively. The final geometry snapshot was taken after the systems equilibrated at ∼1000 ps. (c) Adhesion energy of the three polymers with Si for the coverage of five chains (C5), 10 chains (C10), and 15 chains (C15). (Beige: Si, blue: N, gray: C, and white: H).

**Table 2. Average Orientation of PPAN and PPy Chains on the Si Surface for C5, C10, and C15**

binder	C5 (5 chains) (deg)	C10 (10 chains) (deg)	C15 (15 chains) (deg)
PPAN	77.9	78.8	80.1
PPy	20.7	34.8	40.4
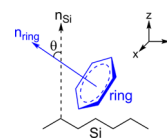
Figure 10. Orientation angle (θ) of the monomer ring with the Si surface.

the chains would bind to the Si surface regardless of the number of chains in the system. In reality, fewer chains are able to bind to the surface because of steric crowding. Figure 11 shows that the effective number of chains bound to the surface decreases from the 100% adsorption case as the coverage increases. This decrease is significantly higher in PPy than in PPAN, strengthening our second hypothesis that fewer PPy chains are able to bind to the Si surface because of the parallel orientation of PPy on the surface.

We next analyze the structure of the bulk polymer interfaces to understand binding mechanisms and the adhesion energy trends for bulk polymers. The position and orientation of every monomer was determined in each simulation of the bulk polymer in contact with the Si surface. Monomers were then
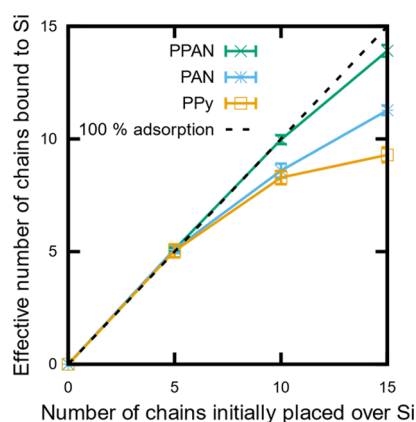
Figure 11. Effective number of chains bound to the Si surface plotted against the number of chains placed in the simulation cell. Data presented are the average of four independent simulations.

distributed in respective bins based on their position in the z direction. For every bin, the average orientation angle of its monomers, as described in Figure 10, is plotted against the position of the center of the bin, shown in Figure 12. The bulk
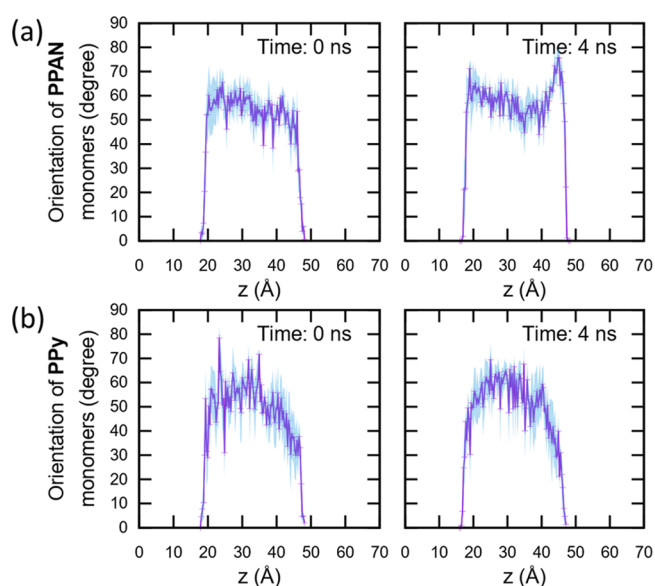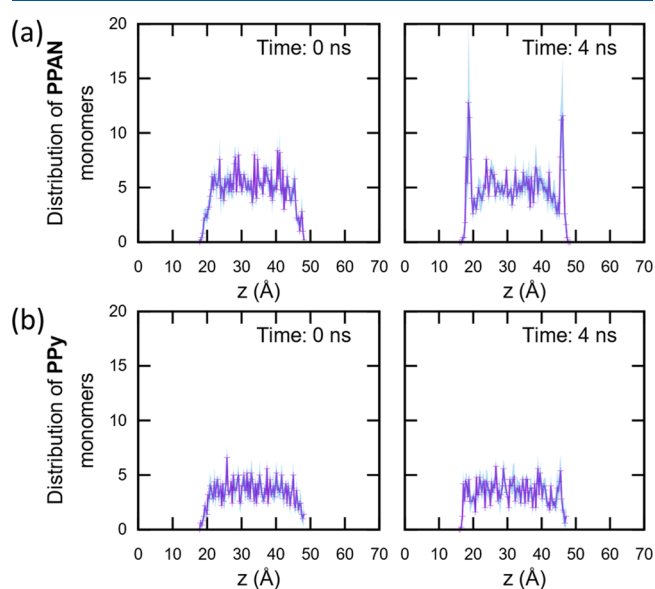

Figure 12. Orientation of monomers (as described in Figure 10) of (a) PPAN and (b) PPy with the z axis at the start (left panels) and end (right panels) of the simulation of Si/bulk polymer composite. Data presented are the average of five independent simulation trials. Shaded area around the data lines represents the standard error of the five trials.

polymer occupies the space in the center of the simulation cell, and so, the two data extremes in Figure 12 represent the top and bottom interfaces of the Si slab. For PPAN, the orientation curve turns from concave to convex as the simulation progresses, indicating higher orientation angles and perpendicular binding at the Si/PPAN interface. For PPy, the orientation curve becomes more concave toward the end of the simulation, indicating lower orientation angles and parallel binding at the Si/PPy interface. This analysis of orientation angles supports our first hypothesis for the adhesion energy trend reversal: the bulk PPy chains bind parallel to the Si

surface and bulk PPAN chains bind perpendicular to the Si surface.

The distribution of monomers along the z direction is shown in Figure 13. More monomers (i.e., more chains) are present at

Figure 13. Distribution of monomers of (a) PPAN and (b) PPy in the z direction at the start (left panels) and end (right panels) of the simulation of the Si/bulk polymer composite. Data presented are the average of five independent simulation trials. Shaded area around the data lines represents the standard error of the five trials.

the Si/PPAN interface compared to the Si/PPy interface, signifying better stacking and more Si/polymer bonding, thus supporting our second hypothesis for the reversal of adhesion energy as the polymer coverage increases. The number of bonds that form at the Si/bulk polymer interface was also quantified, and the data are presented in Table 3 along with

Table 3. Number of Bonds Each Bulk Polymer Makes with Si and its Adhesion Energy

binder	C−Si bonds	H−Si bonds	N−Si bonds	$E_{adhesion}$ (kcal mol^{-1} Å^{-2})
PPAN	13.2	0.0	35.8	−2.3
PAN	5.0	0.0	70.2	−2.3
PPy	14.5	1.1	21.0	−1.9

the adhesion energies. More bonds form at the Si/bulk polymer interface for PPAN and PAN compared to PPy because of the perpendicular orientation and higher coverage of polymer chains on the surface, resulting in stronger overall adhesion even though the single chain of PPy binds more strongly to the Si surface.

4. DISCUSSION

One of the most important performance metrics for a binder is its adhesive strength, as it provides multiple benefits for enhancing the longevity of the electrode. A binder with strong adhesion properties sustains the structural integrity of the electrode during lithiation/delithiation cycling, while stabilizing the SEI layer. It also reduces the irreversible electrolyte decomposition by passivating the surface of the active material. In general, binders are designed by incorporating functional

groups that have strong affinity for the active material. In our study, we have demonstrated that the conformation of these functional groups at the interface is another important design guideline when engineering binder/active material interfaces. As we investigated the adhesion properties of the interfaces between various structural forms of binders and Si, we determined that single chains of PPy have more affinity for the Si surface because the conjugated electrons of the entire ring interact with Si, whereas in PPAN, only the lone pair of the nitrogen interacts with Si. These observations suggest that PPy binds more strongly to the surface; however, the full atomistic treatment of the Si/bulk polymer interface reveals that the parallel binding of PPy chains limits the access of other chains to the surface reducing the overall adhesion energy of bulk PPy. These results are supported by previous experimental studies suggesting that higher binder coverage results in higher peel strength (adhesion strength) at the binder/active material interface in electrodes.[10] As such, we predict that PPAN will achieve higher coverage and better adhesion over Si that will result in a uniform passivation layer (i.e., an artificial SEI), which has been shown in other studies[10,11] to decrease the reductive decomposition of the electrolyte and to improve overall battery performance.

In addition to strong adhesion, an elastic binder is highly preferred as it provides flexibility to the Si/polymer matrix and reduces cracking caused by the build-up of lithiation-induced stress. Separate studies report that PAN and PPy are stiff binders,[10,34,89] yet they work well with Si anodes because of their strong interfacial adhesion properties. Our results show that PPAN is more elastic than both PAN and PPy because of its low Young's modulus. PPAN has better conformation at the Si/PPAN interface that results in higher coverage and, in turn, stronger adhesion to the Si surface. Being more elastic and highly adhesive, our study suggests PPAN to be a superior binder compared to PAN and PPy. Although experimental studies comparing these three polymers would be required to validate our findings, a study by Piper et al.[23] supports our results by showing that conformal coatings of PPAN on nano-Si provide mechanical resilience and reduce cracking and delamination in the electrode.

5. CONCLUSIONS

A ReaxFF Si/C/N/H force field was developed to investigate the interaction of C/N/H-based polymers with Si. Validation of the force field was established by benchmarking the mechanical properties of the polymers predicted with ReaxFF against the data from the literature. The Si/binder interfacial properties of the three polymers (PPAN, PAN, and PPy) were analyzed in various structural forms, ranging from monomers and single chains to bulk polymers. Simulations of monomers and single chain polymers interacting with Si suggest that PPy has strong adhesion to Si because the entire chain bonds to the surface by sharing delocalized electrons with Si via multiple N–Si and C–Si bonds. However, simulations of bulk polymers reveal a counter-intuitive result, where PPAN binds more strongly to the surface than PPy. The analysis of various polymer chain coverages on Si and bulk polymer/Si structures reveals that the perpendicular binding of PPAN allows for better stacking of PPAN chains at the interface, leading to a higher bond density on the surface. Conversely, the parallel binding of PPy, while strong, obstructs other chains from accessing the Si surface resulting in poor overall adhesion.

These results highlight the fact that multiple phenomena are at play and that together they can yield unexpected results. Here, we explored the interfaces of several structural forms of the polymers with Si to elucidate how the binding properties of a single chain does not always translate directly to how the bulk polymer will bind to the surface. The force field and simulation methods developed here are key for understanding atomic-scale interfacial phenomena in these systems, which influence binder adhesion properties and ultimately battery performance. These tools can be applied to screen and identify optimal polymer binders, thus expediting the exploration of novel binders for Si-based Li-ion batteries.

■ ASSOCIATED CONTENT

ⓢ Supporting Information

The Supporting Information is available free of charge on the ACS Publications website at DOI: 10.1021/acs.jpcc.9b08216.

> ReaxFF Si/C/N/H force field development, training sets, and additional results for the mechanical properties of binders and interfacial properties of Si/binder composites (PDF)

■ AUTHOR INFORMATION

Corresponding Author

*E-mail: tsenftle@rice.edu. Phone: +1-713-348-4714.

ORCID ⓘ

Thomas P. Senftle: 0000-0002-5889-5009

Notes

The authors declare no competing financial interest.
The full training set and force field along with the input and output files of MD simulations are available at https://github.com/tsenftle/ReaxFF-SiliconPolymers.

■ ACKNOWLEDGMENTS

■ REFERENCES

(1) Huang, S.; Ren, J.; Liu, R.; Yue, M.; Huang, Y.; Yuan, G. The Progress of Novel Binder as a Non-Ignorable Part to Improve the Performance of Si-Based Anodes for Li-Ion Batteries. *Int. J. Energy Res.* **2018**, *42*, 919–935.

(2) Chen, H.; Ling, M.; Hencz, L.; Ling, H. Y.; Li, G.; Lin, Z.; Liu, G.; Zhang, S. Exploring Chemical, Mechanical, and Electrical Functionalities of Binders for Advanced Energy-Storage Devices. *Chem. Rev.* **2018**, *118*, 8936–8982.

(3) Obrovac, M. N.; Krause, L. J. Reversible Cycling of Crystalline Silicon Powder. *J. Electrochem. Soc.* **2007**, *154*, A103–A108.

(4) Obrovac, M. N.; Christensen, L. Structural Changes in Silicon Anodes during Lithium Insertion/Extraction. *Electrochem. Solid-State Lett.* **2004**, *7*, A93–A96.

(5) Choi, J. W.; Aurbach, D. Promise and Reality of Post-Lithium-Ion Batteries with High Energy Densities. *Nat. Rev. Mater.* **2016**, *1*, 16013.

(6) Zhang, W.-J. A Review of the Electrochemical Performance of Alloy Anodes for Lithium-Ion Batteries. *J. Power Sources* **2011**, *196*, 13–24.

(7) Liu, X. H.; Zheng, H.; Zhong, L.; Huang, S.; Karki, K.; Zhang, L. Q.; Liu, Y.; Kushima, A.; Liang, W. T.; Wang, J. W.; et al. Anisotropic Swelling and Fracture of Silicon Nanowires during Lithiation. *Nano Lett.* **2011**, *11*, 3312−3318.

(8) Lee, S. W.; McDowell, M. T.; Berla, L. A.; Nix, W. D.; Cui, Y. Fracture of Crystalline Silicon Nanopillars during Electrochemical Lithium Insertion. *Proc. Natl. Acad. Sci. U.S.A.* **2012**, *109*, 4080−4085.

(9) Tariq, F.; Yufit, V.; Eastwood, D. S.; Merla, Y.; Biton, M.; Wu, B.; Chen, Z.; Freedman, K.; Offer, G.; Peled, E.; et al. In-Operando X-Ray Tomography Study of Lithiation Induced Delamination of Si Based Anodes for Lithium-Ion Batteries. *ECS Electrochem. Lett.* **2014**, *3*, A76−A78.

(10) Gong, L.; Nguyen, M. H. T.; Oh, E.-S. High Polar Polyacrylonitrile as a Potential Binder for Negative Electrodes in Lithium Ion Batteries. *Electrochem. Commun.* **2013**, *29*, 45−47.

(11) Komaba, S.; Ozeki, T.; Okushi, K. Functional Interface of Polymer Modified Graphite Anode. *J. Power Sources* **2009**, *189*, 197−203.

(12) Lee, J.-H.; Paik, U.; Hackley, V. A.; Choi, Y.-M. Effect of Poly(Acrylic Acid) on Adhesion Strength and Electrochemical Performance of Natural Graphite Negative Electrode for Lithium-Ion Batteries. *J. Power Sources* **2006**, *161*, 612−616.

(13) Schweidler, S.; de Biasi, L.; Schiele, A.; Hartmann, P.; Brezesinski, T.; Janek, J. Volume Changes of Graphite Anodes Revisited: A Combined Operando X-Ray Diffraction and In Situ Pressure Analysis Study. *J. Phys. Chem. C* **2018**, *122*, 8829−8835.

(14) Wilson, A. M.; Dahn, J. R. Lithium Insertion in Carbons Containing Nanodispersed Silicon. *J. Electrochem. Soc.* **1995**, *142*, 326−332.

(15) Lopez, J.; Mackanic, D. G.; Cui, Y.; Bao, Z. Designing Polymers for Advanced Battery Chemistries. *Nat. Rev. Mater.* **2019**, *4*, 312.

(16) Kwon, T.-w.; Choi, J. W.; Coskun, A. The Emerging Era of Supramolecular Polymeric Binders in Silicon Anodes. *Chem. Soc. Rev.* **2018**, *47*, 2145−2164.

(17) Shi, Y.; Zhou, X.; Yu, G. Material and Structural Design of Novel Binder Systems for High-Energy, High-Power Lithium-Ion Batteries. *Acc. Chem. Res.* **2017**, *50*, 2642−2652.

(18) Liu, G.; Xun, S.; Vukmirovic, N.; Song, X.; Olalde-Velasco, P.; Zheng, H.; Battaglia, V. S.; Wang, L.; Yang, W. Polymers with Tailored Electronic Structure for High Capacity Lithium Battery Electrodes. *Adv. Mater.* **2011**, *23*, 4679−4683.

(19) Ma, Y.; Ma, J.; Cui, G. Small Things Make Big Deal: Powerful Binders of Lithium Batteries and Post-Lithium Batteries. *Energy Storage Mater.* **2019**, *20*, 146−175.

(20) Cui, L.-F.; Hu, L.; Wu, H.; Choi, J. W.; Cui, Y. Inorganic Glue Enabling High Performance of Silicon Particles as Lithium Ion Battery Anode. *J. Electrochem. Soc.* **2011**, *158*, A592−A596.

(21) Luo, L.; Xu, Y.; Zhang, H.; Han, X.; Dong, H.; Xu, X.; Chen, C.; Zhang, Y.; Lin, J. Comprehensive Understanding of High Polar Polyacrylonitrile as an Effective Binder for Li-Ion Battery Nano-Si Anodes. *ACS Appl. Mater. Interfaces* **2016**, *8*, 8154−8161.

(22) Thakur, M.; Sinsabaugh, S. L.; Isaacson, M. J.; Wong, M. S.; Biswal, S. L. Inexpensive Method for Producing Macroporous Silicon Particulates (MPSPs) with Pyrolyzed Polyacrylonitrile for Lithium Ion Batteries. *Sci. Rep.* **2012**, *2*, 795.

(23) Piper, D. M.; Yersak, T. A.; Son, S.-B.; Kim, S. C.; Kang, C. S.; Oh, K. H.; Ban, C.; Dillon, A. C.; Lee, S.-H. Conformal Coatings of Cyclized-PAN for Mechanically Resilient Si Nano-Composite Anodes. *Adv. Energy Mater.* **2013**, *3*, 697−702.

(24) Piper, D. M.; Evans, T.; Xu, S.; Kim, S. C.; Han, S. S.; Liu, K. L.; Oh, K. H.; Yang, R.; Lee, S.-H. Optimized Silicon Electrode Architecture, Interface, and Microgeometry for Next-Generation Lithium-Ion Batteries. *Adv. Mater.* **2016**, *28*, 188−193.

(25) Piper, D. M.; Woo, J. H.; Son, S.-B.; Kim, S. C.; Oh, K. H.; Lee, S.-H. Hierarchical Porous Framework of Si-Based Electrodes for Minimal Volumetric Expansion. *Adv. Mater.* **2014**, *26*, 3520−3525.

(26) Shen, L.; Shen, L.; Wang, Z.; Chen, L. In Situ Thermally Cross-linked Polyacrylonitrile as Binder for High-Performance Silicon as Lithium Ion Battery Anode. *ChemSusChem* **2014**, *7*, 1951−1956.

(27) Liu, X. H.; Zhong, L.; Huang, S.; Mao, S. X.; Zhu, T.; Huang, J. Y. Size-Dependent Fracture of Silicon Nanoparticles During Lithiation. *ACS Nano* **2012**, *6*, 1522−1531.

(28) Liu, B.; Soares, P.; Checkles, C.; Zhao, Y.; Yu, G. Three-Dimensional Hierarchical Ternary Nanostructures for High-Performance Li-Ion Battery Anodes. *Nano Lett.* **2013**, *13*, 3414−3419.

(29) Du, F.-H.; Li, B.; Fu, W.; Xiong, Y.-J.; Wang, K.-X.; Chen, J.-S. Surface Binding of Polypyrrole on Porous Silicon Hollow Nanospheres for Li-Ion Battery Anodes with High Structure Stability. *Adv. Mater.* **2014**, *26*, 6145−6150.

(30) Chew, S. Y.; Guo, Z. P.; Wang, J. Z.; Chen, J.; Munroe, P.; Ng, S. H.; Zhao, L.; Liu, H. K. Novel Nano-Silicon/Polypyrrole Composites for Lithium Storage. *Electrochem. Commun.* **2007**, *9*, 941−946.

(31) Guo, Z. P.; Wang, J. Z.; Liu, H. K.; Dou, S. X. Study of Silicon/Polypyrrole Composite as Anode Materials for Li-Ion Batteries. *J. Power Sources* **2005**, *146*, 448−451.

(32) Li, J.; Huang, J. A Nanofibrous Polypyrrole/Silicon Composite Derived from Cellulose Substance as the Anode Material for Lithium-Ion Batteries. *Chem. Commun.* **2015**, *51*, 14590−14593.

(33) Zhou, X.-y.; Tang, J.-j.; Yang, J.; Zou, Y.-l.; Wang, S.-c.; Xie, J.; Ma, L.-l. Effect of Polypyrrole on Improving Electrochemical Performance of Silicon Based Anode Materials. *Electrochim. Acta* **2012**, *70*, 296−303.

(34) Luo, L.; Zhao, P.; Yang, H.; Liu, B.; Zhang, J.-G.; Cui, Y.; Yu, G.; Zhang, S.; Wang, C.-M. Surface Coating Constraint Induced Self-Discharging of Silicon Nanoparticles as Anodes for Lithium Ion Batteries. *Nano Lett.* **2015**, *15*, 7016−7022.

(35) Liu, Y.; Tai, Z.; Zhou, T.; Sencadas, V.; Zhang, J.; Zhang, L.; Konstantinov, K.; Guo, Z.; Liu, H. K. An All-Integrated Anode via Interlinked Chemical Bonding between Double-Shelled-Yolk-Structured Silicon and Binder for Lithium-Ion Batteries. *Adv. Mater.* **2017**, *29*, 1703028.

(36) Seh, Z. W.; Zhang, Q.; Li, W.; Zheng, G.; Yao, H.; Cui, Y. Stable Cycling of Lithium Sulfide Cathodes through Strong Affinity with a Bifunctional Binder. *Chem. Sci.* **2013**, *4*, 3673−3677.

(37) Chen, W.; Qian, T.; Xiong, J.; Xu, N.; Liu, X.; Liu, J.; Zhou, J.; Shen, X.; Yang, T.; Chen, Y.; et al. A New Type of Multifunctional Polar Binder: Toward Practical Application of High Energy Lithium Sulfur Batteries. *Adv. Mater.* **2017**, *29*, 1605160.

(38) Xu, G.; Yan, Q.-b.; Kushima, A.; Zhang, X.; Pan, J.; Li, J. Conductive Graphene Oxide-Polyacrylic Acid (GOPAA) Binder for Lithium-Sulfur Battery. *Nano Energy* **2017**, *31*, 568−574.

(39) Luo, L.; Yang, H.; Yan, P.; Travis, J. J.; Lee, Y.; Liu, N.; Molina Piper, D.; Lee, S.-H.; Zhao, P.; George, S. M.; et al. Surface-Coating Regulated Lithiation Kinetics and Degradation in Silicon Nanowires for Lithium Ion Battery. *ACS Nano* **2015**, *9*, 5559−5566.

(40) Ye, J. C.; An, Y. H.; Heo, T. W.; Biener, M. M.; Nikolic, R. J.; Tang, M.; Jiang, H.; Wang, Y. M. Enhanced Lithiation and Fracture Behavior of Silicon Mesoscale Pillars via Atomic Layer Coatings and Geometry Design. *J. Power Sources* **2014**, *248*, 447−456.

(41) Sandu, G.; Brassart, L.; Gohy, J.-F.; Pardoen, T.; Melinte, S.; Vlad, A. Surface Coating Mediated Swelling and Fracture of Silicon Nanowires during Lithiation. *ACS Nano* **2014**, *8*, 9427−9436.

(42) Min, K.; Kim, Y.; Goyal, S.; Lee, S. H.; McKenzie, M.; Park, H.; Savoy, E. S.; Rammohan, A. R.; Mauro, J. C.; Kim, H.; et al. Interfacial Adhesion Behavior of Polyimides on Silica Glass: A Molecular Dynamics Study. *Polymer* **2016**, *98*, 1−10.

(43) Min, K.; Rammohan, A. R.; Lee, H. S.; Shin, J.; Lee, S. H.; Goyal, S.; Park, H.; Mauro, J. C.; Stewart, R.; Botu, V.; et al. Computational Approaches for Investigating Interfacial Adhesion Phenomena of Polyimide on Silica Glass. *Sci. Rep.* **2017**, *7*, 10475.

(44) Jose, J.; Swaminathan, N. Interfacial Strength Cross-over across Silica- and Graphite-Cis-1,4-Polyisoprene Interfaces. *J. Appl. Phys.* **2018**, *123*, 245306.

(45) Arash, B.; Wang, Q.; Varadan, V. K. Mechanical Properties of Carbon Nanotube/Polymer Composites. *Sci. Rep.* **2015**, *4*, 6479.

(46) Han, Y.; Elliott, J. Molecular Dynamics Simulations of the Elastic Properties of Polymer/Carbon Nanotube Composites. *Comput. Mater. Sci.* **2007**, *39*, 315−323.

(47) Awasthi, A. P.; Lagoudas, D. C.; Hammerand, D. C. Modeling of graphene-polymer interfacial mechanical behavior using molecular dynamics. *Modell. Simul. Mater. Sci. Eng.* **2008**, *17*, 015002.

(48) Lee, S.; Park, J.; Yang, J.; Lu, W. Molecular Dynamics Simulations of the Traction-Separation Response at the Interface between PVDF Binder and Graphite in the Electrode of Li-Ion Batteries. *J. Electrochem. Soc.* **2014**, *161*, A1218−A1223.

(49) Lee, S. Molecular Dynamics Study of the Separation Behavior at the Interface between PVDF Binder and Copper Current Collector. *J. Nanomater.* **2016**, *2016*, 4253986.

(50) van Duin, A. C. T.; Dasgupta, S.; Lorant, F.; Goddard, W. A. ReaxFF: A Reactive Force Field for Hydrocarbons. *J. Phys. Chem. A* **2001**, *105*, 9396−9409.

(51) Raju, M.; Ganesh, P.; Kent, P. R. C.; van Duin, A. C. T. Reactive Force Field Study of Li/C Systems for Electrical Energy Storage. *J. Chem. Theory Comput.* **2015**, *11*, 2156−2166.

(52) Jung, H.; Lee, M.; Yeo, B. C.; Lee, K.-R.; Han, S. S. Atomistic Observation of the Lithiation and Delithiation Behaviors of Silicon Nanowires Using Reactive Molecular Dynamics Simulations. *J. Phys. Chem. C* **2015**, *119*, 3447−3455.

(53) Jung, H.; Yeo, B. C.; Lee, K.-R.; Han, S. S. Atomistics of the Lithiation of Oxidized Silicon (SiOx) Nanowires in Reactive Molecular Dynamics Simulations. *Phys. Chem. Chem. Phys.* **2016**, *18*, 32078−32086.

(54) Yeo, B. C.; Jung, H.; Lee, H. W.; Yun, K.-S.; Kim, H.; Lee, K.-R.; Han, S. S. Atomistic Simulation Protocol for Improved Design of Si-O-C Hybrid Nanostructures as Li-Ion Battery Anodes: ReaxFF Reactive Force Field. *J. Phys. Chem. C* **2017**, *121*, 23268−23275.

(55) Ostadhossein, A.; Kim, S.-Y.; Cubuk, E. D.; Qi, Y.; van Duin, A. C. T. Atomic Insight into the Lithium Storage and Diffusion Mechanism of SiO2/Al2O3 Electrodes of Lithium Ion Batteries: ReaxFF Reactive Force Field Modeling. *J. Phys. Chem. A* **2016**, *120*, 2114−2127.

(56) Ostadhossein, A.; Cubuk, E. D.; Tritsaris, G. A.; Kaxiras, E.; Zhang, S.; van Duin, A. C. T. Stress Effects on the Initial Lithiation of Crystalline Silicon Nanowires: Reactive Molecular Dynamics Simulations Using ReaxFF. *Phys. Chem. Chem. Phys.* **2015**, *17*, 3832−3840.

(57) Kim, K. J.; Wortman, J.; Kim, S.-Y.; Qi, Y. Atomistic Simulation Derived Insight on the Irreversible Structural Changes of Si Electrode during Fast and Slow Delithiation. *Nano Lett.* **2017**, *17*, 4330−4338.

(58) Fan, F.; Huang, S.; Yang, H.; Raju, M.; Datta, D.; Shenoy, V. B.; van Duin, A. C. T.; Zhang, S.; Zhu, T. Mechanical properties of amorphous LixSi alloys: a reactive force field study. *Modell. Simul. Mater. Sci. Eng.* **2013**, *21*, 074002.

(59) Kim, S.-P.; van Duin, A. C. T.; Shenoy, V. B. Effect of Electrolytes on the Structure and Evolution of the Solid Electrolyte Interphase (SEI) in Li-Ion Batteries: A Molecular Dynamics Study. *J. Power Sources* **2011**, *196*, 8590−8597.

(60) Yun, K.-S.; Pai, S. J.; Yeo, B. C.; Lee, K.-R.; Kim, S.-J.; Han, S. S. Simulation Protocol for Prediction of a Solid-Electrolyte Interphase on the Silicon-Based Anodes of a Lithium-Ion Battery: ReaxFF Reactive Force Field. *J. Phys. Chem. Lett.* **2017**, *8*, 2812−2818.

(61) Islam, M. M.; Bryantsev, V. S.; van Duin, A. C. T. ReaxFF Reactive Force Field Simulations on the Influence of Teflon on Electrolyte Decomposition during Li/SWCNT Anode Discharge in Lithium-Sulfur Batteries. *J. Electrochem. Soc.* **2014**, *161*, E3009−E3014.

(62) Saha, B.; Schatz, G. C. Carbonization in Polyacrylonitrile (PAN) Based Carbon Fibers Studied by ReaxFF Molecular Dynamics Simulations. *J. Phys. Chem. B* **2012**, *116*, 4684−4692.

(63) Saha, B.; Furmanchuk, A. o.; Dzenis, Y.; Schatz, G. C. Multi-Step Mechanism of Carbonization in Templated Polyacrylonitrile Derived Fibers: ReaxFF Model Uncovers Origins of Graphite Alignment. *Carbon* **2015**, *94*, 694−704.

(64) Mortier, W. J.; Ghosh, S. K.; Shankar, S. Electronegativity-Equalization Method for the Calculation of Atomic Charges in Molecules. *J. Am. Chem. Soc.* **1986**, *108*, 4315−4320.

(65) Chenoweth, K.; van Duin, A. C. T.; Goddard, W. A. ReaxFF Reactive Force Field for Molecular Dynamics Simulations of Hydrocarbon Oxidation. *J. Phys. Chem. A* **2008**, *112*, 1040−1053.

(66) Senftle, T. P.; Hong, S.; Islam, M. M.; Kylasa, S. B.; Zheng, Y.; Shin, Y. K.; Junkermeier, C.; Engel-Herbert, R.; Janik, M. J.; Aktulga, H. M.; et al. The ReaxFF Reactive Force-Field: Development, Applications and Future Directions. *npj Comput. Mater.* **2016**, *2*, 15011.

(67) Newsome, D. A.; Sengupta, D.; Foroutan, H.; Russo, M. F.; van Duin, A. C. T. Oxidation of Silicon Carbide by O2 and H2O: A ReaxFF Reactive Molecular Dynamics Study, Part I. *J. Phys. Chem. C* **2012**, *116*, 16111−16121.

(68) van Duin, A. C. T.; Baas, J. M. A.; van de Graaf, B. Delft Molecular Mechanics: A New Approach to Hydrocarbon Force Fields. Inclusion of a Geometry-Dependent Charge Calculation. *J. Chem. Soc., Faraday Trans.* **1994**, *90*, 2881−2895.

(69) Valiev, M.; Bylaska, E. J.; Govind, N.; Kowalski, K.; Straatsma, T. P.; Van Dam, H. J. J.; Wang, D.; Nieplocha, J.; Apra, E.; Windus, T. L.; et al. NWChem: A Comprehensive and Scalable Open-Source Solution for Large Scale Molecular Simulations. *Comput. Phys. Commun.* **2010**, *181*, 1477−1489.

(70) Becke, A. D. A new mixing of Hartree-Fock and local density-functional theories. *J. Chem. Phys.* **1993**, *98*, 1372−1377.

(71) Grimme, S.; Antony, J.; Ehrlich, S.; Krieg, H. A Consistent and Accurate Ab Initio Parametrization of Density Functional Dispersion Correction (DFT-D) for the 94 Elements H-Pu. *J. Chem. Phys.* **2010**, *132*, 154104.

(72) Müller, J.; Hartke, B. ReaxFF Reactive Force Field for Disulfide Mechanochemistry, Fitted to Multireference Ab Initio Data. *J. Chem. Theory Comput.* **2016**, *12*, 3913−3925.

(73) Kresse, G.; Furthmüller, J. Efficiency of Ab-Initio Total Energy Calculations for Metals and Semiconductors Using a Plane-Wave Basis Set. *Comput. Mater. Sci.* **1996**, *6*, 15−50.

(74) Chadi, D. J. Atomic and Electronic Structures of Reconstructed Si(100) Surfaces. *Phys. Rev. Lett.* **1979**, *43*, 43−47.

(75) Perdew, J. P.; Burke, K.; Ernzerhof, M. Generalized Gradient Approximation Made Simple. *Phys. Rev. Lett.* **1996**, *77*, 3865−3868.

(76) Kresse, G.; Joubert, D. From Ultrasoft Pseudopotentials to the Projector Augmented-Wave Method. *Phys. Rev. B: Condens. Matter Mater. Phys.* **1999**, *59*, 1758−1775.

(77) Monkhorst, H. J.; Pack, J. D. Special Points for Brillouin-Zone Integrations. *Phys. Rev. B: Solid State* **1976**, *13*, 5188−5192.

(78) Plimpton, S. Fast Parallel Algorithms for Short-Range Molecular Dynamics. *J. Comput. Phys.* **1995**, *117*, 1−19.

(79) Evans, D. J.; Holian, B. L. The Nose-Hoover thermostat. *J. Chem. Phys.* **1985**, *83*, 4069−4074.

(80) Verlet, L. Computer "Experiments" on Classical Fluids. I. Thermodynamical Properties of Lennard-Jones Molecules. *Phys. Rev.* **1967**, *159*, 98−103.

(81) Xue, T. J.; McKinney, M. A.; Wilkie, C. A. The Thermal Degradation of Polyacrylonitrile. *Polym. Degrad. Stab.* **1997**, *58*, 193−202.

(82) Rahaman, M. S. A.; Ismail, A. F.; Mustafa, A. A Review of Heat Treatment on Polyacrylonitrile Fiber. *Polym. Degrad. Stab.* **2007**, *92*, 1421−1432.

(83) Ko, T.-H. The Influence of Pyrolysis on Physical Properties and Microstructure of Modified PAN Fibers during Carbonization. *J. Appl. Polym. Sci.* **1991**, *43*, 589−600.

(84) Hurley, R. B.; Tzentis, L. S. Density of Polyacrylonitrile. *J. Polym. Sci., Part B: Polym. Lett.* **1963**, *1*, 423−426.

(85) Gupta, N.; Rai, R.; Sikder, A.; Nandi, S.; Tanwar, A.; Khatokar, R.; Pask, S. D.; Mitra, S. Design and Development of a Poly-(Acrylonitrile-Co-Methyl Methacrylate) Copolymer to Improve the Viscoelastic and Surface Properties Critical to Scratch Resistance. *RSC Adv.* **2016**, *6*, 37933−37937.

(86) Rabias, I.; Hamerton, I.; Howlin, B. J.; Foot, P. J. S. Theoretical Studies of Conducting Polymers Based on Substituted Polypyrroles. *Comput. Theor. Polym. Sci.* **1998**, *8*, 265−271.

(87) Cuenot, S.; Demoustier-Champagne, S.; Nysten, B. Elastic Modulus of Polypyrrole Nanotubes. *Phys. Rev. Lett.* **2000**, *85*, 1690−1693.

(88) Poisson, S.-D. *Traité De Mécanique*; Mme veuve Courcier: Paris, 1811.

(89) Pan, L.; Chortos, A.; Yu, G.; Wang, Y.; Isaacson, S.; Allen, R.; Shi, Y.; Dauskardt, R.; Bao, Z. An Ultra-Sensitive Resistive Pressure Sensor Based on Hollow-Sphere Microstructure Induced Elasticity in Conducting Polymer Film. *Nat. Commun.* **2014**, *5*, 3002.